Crystallization mechanism of BaO-CaO-Al2O3-SiO2 (BCAS) glass thin-films

T. Carlier, Renaud Podor, S. Saitzek, Lionel Montagne, P. Roussel, F.O. Méar

Crystallization mechanism of $BaO-CaO-Al_2O_3-SiO_2$ (BCAS) glass thin-films

T. Carlier [a], R. Podor [b], S. Saitzek [c], L. Montagne [a], P. Roussel [a], and F.O. Méar [a,*]

[a] Univ. Lille, CNRS, Centrale Lille, Univ. Artois, UMR 8181 - UCCS - Unité de Catalyse et Chimie du Solide, F-59000 Lille, France.

[b] ICSM, CEA, CNRS, ENSCM, Univ. Montpellier, Marcoule, France.

[c] Univ. Artois, CNRS, Centrale Lille, Univ. Lille, UMR 8181, Unité de Catalyse et Chimie du Solide (UCCS), F-62300 Lens, France.

* *Corresponding author*: francois.mear@univ-lille.fr

Abstract

Crystallization pathways of BaO-CaO-Al_2O_3-SiO_2 (BCAS) glass were determined as a function of time and temperature, using a set of adapted and *in-situ* characterization techniques such as differential thermal analysis, high-temperature X-ray diffraction, nuclear magnetic resonance and high-temperature environmental scanning electron microscopy. Glass systems are a melted quenched bulk form and a deposited thin-film form (Pulsed Laser Deposition technique was used to obtain a coating on Si-substrate with a thickness up to 100 nm). The composition of the crystallized phases depends on the geometry of the glass, and of the applied geometrical constraints. These constraints control the volume fraction of crystallized glass melt as a function of time and temperature, and thus modify the reactional pathways.

Keywords

Glass thin-film; Bulk glass; Crystallization; SS-NMR; HT-ESEM

1. Introduction

The development of glassy materials as thin-films has a growing interest due to their large potential application in numerous domains. For instance, they can be found as bioactive coatings [1, 2] allowing to improve tissue repair [3] or the creation of scaffolds for bone regeneration [4]; chalcogenide glasses are used for infrared detectors, lenses [5, 6], infrared optical waveguides [7, 8] or photonic devices [9], and more recently, for photovoltaic solar cell materials [10]. On their side, aluminosilicate glasses are known to withstand high temperatures and have a high resistance to thermal and mechanical shock, chemical attack and oxygen permeation [11]. Deposited as thin-films, they can thus be attractive for protective coating for high temperature applications [12], dielectric layer in the packaging of semiconductors [13], planar waveguide or as phosphor layers [14], or sealing glass towards miniaturized SOFC technology.

Glassy thin films can be obtained by many several methods: sedimentation, electrostatic deposition, sol–gel technology, precipitation from the vapor phase, vacuum deposition, among others. [15-26]. Each of these methods, especially those where the initial material is subjected to a high-energy effect, has a specific influence on the physico-chemical properties of the resulting films. Therefore, it is not always possible to specify any correlation between the properties of bulk glasses and those of thin films based on these glasses. Pulsed Laser Deposition (PLD) is a versatile technique in which it is relatively easy to adapt the operating parameters to the type of coating to be deposited [27]. In addition, one of the main advantages of this technique is its good transfer of the stoichiometry of a multicomponent target to the deposited film [28].

In a previous work, due to their high thermal properties such as T_g up to 750°C, we formulated BCAS glass for a use as sealant in Solid Oxide Fuel Cells (SOFCs) [29]. A concept of self-healing was also developed to self-repair and prevent leakage, by restoring the mechanical integrity of the parent glass at operating temperature 650-800°C without external intervention [29-31]. Finally, on the basis of this process developed for massive devices, we have developed an ultra-thin coating elaboration process

adapted to high temperature self-healing applications for aeronautics [32]. In this context, since BCAS glass is subjected to high temperatures, we need to understand its behavior (structure, properties) in such conditions, more especially to study the crystallization properties of both bulk and thin-film glasses as a function of temperature.

The Johnson-Mehl-Avrami (JMA) equation describes the kinetics of phase transformation, such as crystallization of a glass, at a constant temperature [33]:

$$-Ln(1-x) = (kt)^n$$

Where, x is the volume fraction of the glass crystallized after time t, n the dimensionless Avrami exponent which reflects the growth morphology (one-, two- or three-dimensional growth) and k the reaction rate constant. The temperature dependence of k (at least within narrow temperature ranges) follows an Arrhenius equation:

$$k = \nu . \exp(-\frac{E}{RT})$$

Where E is the effective overall activation energy for the transformation process, ν an effective frequency factor which reflects the probability that a molecule having energy E participates in the transformation, R the gas constant and T the absolute reaction temperature.

The crystallization kinetics in the BCAS glass composition were described by Bansal *et al.* [34] and showed an Avrami exponent n = 2.6 which corresponds to a crystallization in 3 dimensions. The question arises about the crystallization mechanisms on glasses deposited as thin layers.

Few works are devoted in the literature on the thin-film glass crystallization and particularly of oxide glasses. In metallic glasses, it was shown that crystallization behavior of thin-films is very different from that of bulk glasses [35]. The nanocrystals structure in the film above crystallization temperature was attributed to the high nucleation rate and low nucleus growth rate in the crystallization process. White *et al.* [36] showed the difference of crystallization mechanism in chalcogenide glass between bulk and thin-film forms. The crystallization initiated in volume for the bulk was at the surface in thin-film, thus the films crystallized much faster, even though the apparent energy was higher in films.

The objective of this work is to study the mechanism of crystallization for such a glass system in both melt quenched bulk form and thin-film form. In a first step, bulk glasses were synthesized and thoroughly characterized using different complementary techniques such as Differential Thermal Analysis (DTA), High-Temperature X-Ray Diffraction (HT-XRD), High-Temperature Environmental Scanning Electron Microscopy (HT-ESEM) and solid state Nuclear Magnetic Resonance (NMR). In a second step, PLD technique was used to obtain coatings of the same formulation on Si-substrates with a thickness up to 100 nm [37] and were afterward characterized using the same technics.

2. Experimental procedure

In Coillot *et al.* [29], the experimental conditions of BCAS bulk glass synthesis used in this study are reported. Glass thin films were prepared by Pulsed Laser Deposition (PLD) on silicon substrates, using conditions described elsewhere [37]. In this previous study, those thin films were characterized by various methods such as X-ray Photoelectron Spectroscopy (XPS), Time of Flight Secondary Ion Mass Spectrometry (ToF-SIMS), Atomic Force Microscopy (AFM) and Spectroscopic Ellipsometry (SE). XPS and ToF-SIMS results have highlighted a stoichiometric transfer and a good homogeneity of the layers obtained by PLD. Additional TEM analysis showed that thin films (Figure 1 (a), 100 nm thick) have an amorphous structure (Figure 1 (b)), an absence of nano-crystallite and a good quality of glass / substrate interface.

Characteristic temperatures, reported in Table 1, were obtained by Differential Thermal Analysis (DTA) using a Setsys Evolution (SETARAM DTA 92-16.18) under air with a heating rate of 10 °C/min [29].

The crystallization process of both bulk and thin-films glasses was followed using a Rigaku SmartLab high resolution or high flux X-ray diffractometer equipped with a 9 kW rotating anode X-ray generator delivering copper radiation (λ K_α = 1.5418 Å). Since the amount of active material on 100 nm thin-film is very low, we decided to use a high-flux Bragg-Brentano geometry configuration instead of high-resolution. However, to avoid any saturation of the detector by the extremely intense peak of the

single crystal silicon substrate, we choose to misalign it by 2°, a sufficient value to significantly decrease the non-useful huge peak-intensity of the silicon wafer, but allowing to see the other peaks issued from the active materials. Bulk and thin films were studied using this configuration, even if for bulk, this 2° misalignment is not useful. The scans were performed in the range of 10°-50°, with a step size of 0.02° and a speed of 1 °C/min. This device allows *in-situ* temperature measurements up to 1100 °C using an Anton Paar DHS 1100 heating rate. Based on the DTA data, we carried out the heat treatment presented in Figure 2 for the in-situ crystallization monitoring by High-Temperature X-Ray Diffraction (HT-DRX).

The heat treatment consists of four steps:

(1) A fast heating rate (10 °C/min) from ambient to glass transition temperature T_g = 770 °C where no crystallization phenomenon was expected;

(2) A second step with a slower rise (1 °C/min.) from T_g = 770 °C to T_x = 960 °C (onset crystallization temperature), where, at this stage, the crystallization temperature was reached at T_x;

(3) A 10 h isothermal treatment at T_x = 960 °C leaving the growth of the crystals;

(4) A controlled temperature (2 °C/min) drop to the ambient in order to observe if no structural change occurs during sample cooling.

The NMR spectra of ^{29}Si were performed at 19.9 MHz on a 2.35 T spectrometer equipped with a 7 mm probe with a rotation frequency of 5 kHz. In order to obtain an acceptable signal-to-noise ratio, we used the following parameters: 64 acquisitions with a relaxation time of 150 s. The reference used is a tetramethoxysilane solution (TMS). For the ^{27}Al nucleus, the NMR spectra were recorded at 208.5 MHz on an 18.8 T spectrometer equipped with a 3.2 mm probe with a 20 kHz rotation frequency. Here, to get a proper signal-to-noise ratio, we used the following parameters: 1024 acquisitions with a relaxation time of 2 s. The reference used for this nucleus is $Al(NO_3)_3$. The NMR spectrum of ^{29}Si of the glass before crystallization has a resonance centered on - 85 ppm. This characteristic appearance of a disordered material is induced here by the multiplicity of characteristics chemical bonds around silicon (Si-O bond lengths and angles), which generate different environments.

The High-Temperature Environmental Scanning Electron Microscopy (HT-ESEM) experiments were performed using a HT1400 heating stage attached to a Quanta 200 ESEM FEG (FEI Company) microscope. The main operating conditions were a 30 kV accelerating voltage under a 200 Pa air pressure. For both experiments, the heating rate was 30 °C/min up to 750 °C, then 5 °C/min up to 850 °C and finally 2 °C/min up to the isothermal temperature. The isothermal temperatures were 1000 °C and 1070 °C for bulk and thin film experiments respectively. The run durations at the isothermal plateau were 40 min and 105 min for bulk and thin film experiments respectively. Image processing was performed using ImageJ software [38]. The SIFT plugin was used for image stack alignments and Trainable Weka Segmentation plugin was used for image segmentation [39, 40].

3. Results

3.1. BCAS bulk glass

The XRD patterns obtained during the HT-XRD analyzes for the solid material are reported on Figure 3 (a). Indexing of the different crystalline phases is performed using EVA software and is presented in Figure 3 (b).

From Figure 3, no crystallization is observed up to 940 °C, the glass still fully amorphous. From this temperature, several peaks begin to appear on the XRD, the most intense being located at 11.2°. It is attributed to the well-known hexacelsian phase $BaAl_2Si_2O_8$ [41, 42]. Then, as soon as the temperature reaches 960 °C, new peaks are visible and indicate the formation of several crystalline phases. Indeed, the peaks located at 24.9°; 25.8° and 26.6° are characteristic of the barium metasilicate ($BaSiO_3$) structure [42]. The other peaks located at 29.9° and 30.6° are associated to the formation of calcium metasilicate ($CaSiO_3$) and mixed barium and calcium orthosilicate ($Ba_xCa_{2-x}SiO_4$) respectively. During the isothermal plateau at 960 °C, no additional phase is formed, but only the growth of the already crystallized phases. After 10 h of isothermal treatment at 960 °C, the main phase observed remains the hexacelsian $BaAl_2Si_2O_8$. This result is consistent with already reported studies in the literature

relative to the crystallization of barium and calcium aluminosilicate glass [41]. Note finally that no change is observed during the cooling step.

In order to provide complementary response to XRD analyzes, we decided to probe the ^{29}Si and ^{27}Al nuclei. Figure 4 shows the results of NMR studies performed on a glass powder before and after crystallization (with a heat treatment similar to that previously used for the HT-XRD study).

After heat treatment, the disappearance of the peak on the as-prepared glass (Figure 4 (a)) is accompanied by the appearance of finer peaks. It attests to a reorganization of the network: the glass is crystallized. According to the literature, the intense peaks located at -88.1 and -80.0 ppm can be attributed to hexacelsian ($Ba_2Al_2Si_4O_8$) and barium- and calcium-metasilicates ($BaSiO_3$ & $CaSiO_3$), respectively [43-45]. Crossing with XRD results, the peak located around -75.9 ppm can reasonably be attributed to the last phase which formation was observed, namely $Ba_xCa_{2-x}SiO_4$ orthosilicate. We can also note the systematic presence of other smaller peaks (-82.3 and -91.0 ppm) as well as shoulders at the feet of the three most intense resonance bands. We can hypothesize that during the heat treatment, solid solutions were formed (with Ba / Ca exchanges in crystal structures) but that the cationic exchanges were too limited to be observed by XRD. Regarding the ^{27}Al nucleus, the NMR spectrum recorded before crystallization has a wide asymmetric band (typical of a quadrupole nucleus) whose maximum is located around 55.0 ppm. This band is induced by the chemical and geometric disorder of the glass network. After the heat treatment, we can observe a thinning of this band which attests to the reorganization of the network. This resonance, centered around -56.3 ppm, is attributed to Al atoms in fourfold coordination in the hexacelsian structure.

A HT-ESEM experiment was performed on an almost flat small piece of bulk glass (2 mm^2). This has limited the sample displacements when the transformations have occurred. Therefore, the high magnification observations were always performed on the same region of interest. This however allows to describe precisely the continuity of the transformations and to propose a chemical

transformation pathway. The crystallization process can be described into three distinct steps (Figure 5).

Step 1 – A first crystallization of small X1 crystals (few tens of nanometers) takes place at the surface of the sample begins at T = 850 °C. These crystals grow up to reach approximately 100-250 nm long at T = 920 °C. The quantity of crystals remains relatively low and the maximum surface coverage is below 5.5 %. Then these crystals begin to dissolve in the bulk at T = 950 °C (Figure 5 (b) and Suppl. File 1).

Step 2 – At this temperature, a second type of X2 crystals begins to form in the zones where previous crystals has grown. Then, they grow at the sample surface. Since the collected signal contains a contribution of back scattered electrons, it can be derived that these crystals are composed by lighter elements than the matrix atomic number average. At the center of each X2 crystal, a X3 crystal of a heavier phase also grow (Figure 5 (c)). Regarding their position as well as their grey level, the X3 crystals could be the same composition than the X1 crystals.

Step 3 – A third crystallization finally takes place when the isothermal plateau at T = 1070 °C is reached. The small white X3 crystals that were present inside the crystals grown during Step 2 are the nucleus for the growing X3 crystals (Figure 5 (d)). Furthermore, in the same time, a forth type of crystals (X4) nuclei and grow inside X2 crystals (see the white arrows on Figure 5 (d)). In the same time, a fifth type of crystals (X5) grow inside the remaining liquid (black arrows on Figure 5 (d)). As the X3 crystals growth seems to be limited by the border of the X2 crystals, the growth of the X5 crystals continues up to the quasi complete coverage of the sample surface. The nucleation and growth of these crystals generate steric interactions and deform the sample surface. At the end of the recrystallization plateau, the glass ceramic is solid and the composition of the remaining glass seems to have been sufficiently modified to be solid. All these transformations are clearly visible on movies given as Supplementary Files 2 and 3. On those movies, the sample deformations due to the phase crystallization are clearly observable up to 1 h after the isothermal plateau is reached (formation of valleys, motion of crystals at the glass

melt surface). After this duration, the density of crystals, at the surface and probably in the bulk of the material, is high enough to freeze the crystals' configuration.

As no Energy Dispersive X-ray Spectroscopy (EDS) analysis can be performed in this high temperature configuration, the composition of the different crystals has not been measured during the experiment. An attempt to determine the crystal compositions by comparing their relative average atomic numbers (which is proportional to the number of backscattered electrons emitted by the chemical phase) was done by classifying the average grey level of each phase and comparing the relative average atomic numbers of the phases identified from X-ray diffractograms. Even if the correspondence is not obvious, X1 and X3 compositions could be $BaAl_2Si_2O_8$ whereas X4 could be $CaSiO_3$ and X5 could be $Ba_xCa_{2-x}SiO_4$.

As HT-ESEM allows to observe the formation of phases that arise at the sample surface, some of the crystals that can form in the bulk of the glass melt may not be observed at the sample surface. Conversely, some crystals that are formed at the sample surface (and that are observed by HT-ESEM) may not form in the bulk of the glass melt. Then, some tiny modifications such as those reported above may not be detectable by XRD as the currently admitted detection limit for this technique is approximately a 5 % phase concentration in the analyzed volume. Thus some sample bulk transformations can be observed by XRD and not by HT-ESEM, and reversely, some transformations that take place at the sample surface can be observed by HT-ESEM and not by XRD. Thus, both sets of data should be considered as complementary and they should not be opposed.

The total coverage of the glass by crystals can also be determined by image processing (using ImageJ software). This parameter can give information regarding the variation of the crystal fraction inside the glass-ceramic as a function of time, during the heat treatment. The results are reported on Figure 6. They indicate that the percentage of area covered by crystals increases according to a sigmoid law, *i.e.* according to a Johnson-Mehl-Avrami law.

3.2. BCAS glass thin-film

The XRD patterns obtained during the HT-XRD analyzes for the thin-film glass are shown in Figure 7 (a). As before, the indexing of the different crystalline phases is carried out using the EVA software and is presented in Figure 7 (b).

In the case of thin-film material, we can observe that the X-ray diffractograms are much noisier than for bulk material, which is explained by the small amount of material present (glass thin-film thickness is 100 nm). The tiny peaks located at 28.3°; 32.9°; 35.8° and 37.8° are due to the diffraction of the sample holder. The X-ray diffractograms indicate that the film has an amorphous structure up to 870 °C. From this temperature, we can observe the emergence of several peaks showing the devitrification of the material by the formation of two crystalline phases, namely $Ba_3Si_5O_{13}$ and $CaAl_2SiO_8$. Then, at 960°C we can notice the formation of new peaks at 21.9° and 39.9° indicating the formation of $BaSi_2O_5$. This last phase seems to be formed from the first phase of barium silicate observed ($Ba_3Si_5O_{13}$). Indeed, the evolution of XRD patterns shows the disappearance of $Ba_3Si_5O_{13}$ after 1 h at 960 °C accompanied by an increase of the peak's intensities attributed to $BaSi_2O_5$. This structural evolution of barium silicates has already been demonstrated by Hamnabard *et al.* [46]. In fact, in their work on the temperature behavior of glass-ceramic of the $BaO\text{-}SiO_2\text{-}B_2O_3$ system, they were able to observe, despite a different temperature scheme, at first the formation of $Ba_3Si_5O_{13}$ (after 20 min at 820 °C) then a progressive structural rearrangement until the complete disappearance of this phase, and its replacement by $BaSi_2O_5$ (after more than 30 min at 910 °C.). Thus, in the present work, after 10 h at 960 °C, two crystalline phases are present: $BaSi_2O_5$ as the majority one and $CaAl_2Si_2O_8$ as minority. Finally, as with bulk sample, no structural changes were observed during cooling.

To complete the structural analyzes on the crystallization of thin vitreous layers, the crystallization process was observed using in situ by HT-ESEM. The heat treatment that was performed in the ESEM is the same than the one described above (Figure 1). Micrographs that are representative of the observed phenomena are reported in Figure 8. The complete movie is available as Supplementary File 4.

From the micrographs, a first growth of crystals is starting at about 880 °C, whose shapes is not well defined, indicating that they are probably embedded inside the thin glass melt layer. These crystals grow very fast and they cover the complete volume of the thin-film. This result is consistent with the data obtained by XRD, the first crystallization which begins at T > 870 °C being attributed to the formation of crystals of anorthite ($CaAl_2Si_2O_8$) and barium silicate ($Ba_3Si_5O_{13}$). Their growth continues beyond 900°C. When the temperature reaches 920 °C, a second type of crystals begins to be observable at the sample surface. These crystals grow from the already existing crystals, which appears to act as the main nucleation sites [46]. These observations confirm the structural changes observed during the XRD analyzes, *i.e.* a rearrangement from the $Ba_3Si_5O_{13}$ phase to a $BaSi_2O_5$ phase which takes place at 960 °C. These needle-like shaped barium silicates [47] continue to grow until covering almost the entire surface after 10 h at 960 °C. These various observations are in good agreement with the crystallization process deduced from HT-XRD analyzes.

The percentage of area covered by the crystals can be determined from image analyzes. The results are reported on Figure 6, considering both crystallization processes independently. The first crystallization of anorthite and barium silicate yields to a quasi-complete coverage of the thin film, *i.e.* almost 60% of the thin layer volume was crystallized (assuming that in a thin film, the percentage of area covered is equivalent to the percentage of volume transformed). The size of the crystals (which is approx. 800 nm on the first image where these crystals can be observed) being much larger than the thickness of the thin-film (100 nm), these crystals probably grow in the whole thickness of the thin-film. The second crystallization begins while the first one has reached an equilibrium state. Thus, the percentage of area covered by the second population increases linearly with the duration of the heat treatment. The crystals seems to grow more at the surface and out of the volume of the thin-film glass. In this case, the transformation does not satisfy the JMA law as no sigmoid curve is drawn. This comforts the hypothesis that crystals of $BaSi_2O_5$ do not crystallize in the bulk but that their formation results from the transformation of crystals previously formed. The entire thin-film surface is covered

after the 10 hours heat treatment, but from the curve reported on Figure 6, the whole sample surface should be fully transformed within 3 h.

A 3D representation of the transformation processes is reported on Figure 9 (see also Supplementary File 5). It allows to visualize the first $Ba_3Si_5O_{13}$ crystals formation, and to see how the $BaSi_2O_5$ crystals nucleate from the previously grown $Ba_3Si_5O_{13}$ crystals. Only few $BaSi_2O_5$ crystals begins to grow at the same temperature, and no new nuclei form at higher temperature / longer time, thus strengthening the hypothesis that these crystals do not form in the glass melt.

4. Discussions

HT-XRD analyzes allowed us to highlight the different behavior of crystallization processes between bulk and thin-layer glasses. To discuss these structural changes, we have quantified the degree of polymerization of the different species encountered. Several authors, in particular Mysen *et al.* [48], have defined the degree of polymerization of a glassy network as the number of non-bridging oxygen carried by the tetrahedral cations of the network glassy, noted NBO / T (Non-Bridging Oxygens per Tetrahedron). Calculation of the NBO / T ratio is carried out as follows: the composition of the glass is expressed in molar percentage and we consider then the set of modifying cations which are not compensators of the tetrahedra [AlO_4]. In the present case of BCAS glass, considering that Al is exclusively in a fourfold coordination, this yields the following equation:

$$\frac{NBO}{T} = \frac{2\,(CaO + BaO) - 2\,Al_2O_3}{SiO_2 + 2\,Al_2O_3}$$

From this NBO / T ratio, it is possible to apply a nomenclature system known as the notation Q^n, which expresses the number of bridging oxygens per tetrahedron by the value of n, which is the number of bridging oxygen atoms. An Al tetrahedron that is fully connected to the network by 4 bridging oxygen will then be designated as a Q^4 unit and conversely, an isolated tetrahedron without bridging oxygen will be noted Q^0. The calculation of the index n is done according to the following equation:

$$n = 4 - \frac{NBO}{T}$$

This Q^n notation is generally preferred to the NBO / T ratio because it allows more visualization network connectivity. The value of n, ranging between 0 and 4, indicates that the network is fully polymerized when this parameter is equal to 4. On the contrary a zero value of n expresses a network fully depolymerized. The schematic representation of the nomenclature is presented in Figure 10 (a) in the case of a BCAS glass. Figure 10 (b) summarizes the main results obtained during this study. The widths of the boxes represent an approximate relative proportions of the crystalline phases.

Data obtained from NMR confirm the results obtained by XRD, but they bring complementary information concerning the minor phases. It should also be noted that NMR spectra of the crystallized samples indicates that very low quantity of amorphous phase remains present at the end of the experiment. This result is also confirmed by the direct observation of the sample surface at the end of the heat treatment (HT-ESEM study).

In the case of bulk glass, the first phase that crystallizes at 940 °C during the heat treatment is the hexacelsian with composition $BaAl_2Si_2O_8$. We can reasonably assume that this is the most stable phase under the thermodynamic and kinetic conditions used. With a structural unit Q^4, this phase is therefore more polymerized than the initial glass network. The residual glass melt therefore becomes less polymerized. When the temperature reaches 960 °C, the formations of calcium silicate (Q^2) and barium silicate (Q^2), and in a less extend mixed barium- and calcium-silicate (Q^0), are therefore consistent with the structure of residual glass melt. During the isothermal plateau at 960 °C, the formed phases continue their growing process and no other crystal phase is formed. Thus, at the end of the heat treatment, the hexacelsian main phase, fully polymerized (Q^4), is compensated by the presence of compounds with Q^2, and in a lesser measure, in Q^0, (barium and / or calcium silicates) structural units. It should be noted that the quantity of residual glass after the isothermal heat treatment was not precisely determined. However, the percent area covered by crystals that was determined from the HT-ESEM images indicates that crystallization in glass melt is probably complete. This is consistent with

the measures performed by NMR analyzes of the solid after sample cooling which indicate that the glass is fully transformed.

In the case of thin-film glass, it was unfortunately not currently possible to carry out solid state NMR measurements because the quantity of sample is too low. X-ray diffraction analysis shows that the structural evolution, during crystallization, differs greatly from what has been observed during the study of the bulk glass. Indeed, the formation of a metastable structure of barium-silicate ($Ba_3Si_5O_{13}$) of motif $0.8Q^3 + 0.2Q^2$ as well as the Ca-hexacelsian formation of motif Q^4 was first observed. The simultaneous formation of these phases allows to keep an average Q^3 structural unit. Subsequently, when the temperature reaches 960°C, the metastable phase disappears and seems to act as a germ of crystallization (Figure 9) for the formation of a more stable phase of barium-silicate ($BaSi_2O_5$). The structural unit of this phase is Q^3. This phase is majority at the end of the heat treatment. We can also see the growth of calcium hexacelsian after one hour of treatment at 960 °C. So it seems that the structural units of the crystalline phases remain close to those of the parent glass (Q^3). With regards to the large number of parameters that can influence the crystallization process, it is not easy to explain the differences observed during crystallization in a bulk glass and in thin glass layer. If we take into account structural arguments, we can suggest that the network of the thin glass film is geometrically constrained and that the reorganization of the structural units is rapidly limited. Indeed, the initial formation of large crystals creates the formation of small isolated glassy zones. In these small zones, the structure of the melt remains the same than the one of the parent melt, *i.e.* Q^3. This induces an evolution towards phases with structures that are similar to the one of the initial glass melt network, *i.e.* Q^3.

Contrarily, the network reorganization in the bulk glass melt is not constrained as long as the zones of glass melt remain connected. Thus, chemical species can diffuse in the remaining glass melt and yields to its homogenization and stabilization with the crystals that are formed. Then, the glass melt is first reorganized in Q^4, then in Q^2, according to the sequence of stable phases that are formed, and according to thermodynamic or kinetic criteria.

5. Conclusions

Crystallization pathways of BaO-CaO-Al_2O_3-SiO_2 (BCAS) glass, as a bulk material or deposited as a 100 nm thin-film, were determined as a function of time and temperature, using a set of adapted and *in-situ* characterization techniques.

When the glass is studied as a bulk material, the sequence of phases that form during the heat treatment is **(i)** from 940°C, the celsian $BaAl_2Si_2O_8$ major phase, **(ii)** from 960°C, the $BaSiO_3$, $CaSiO_3$ and $Ba_xCa_{2-x}SiO_4$ minor's phases. Thus, the crystals seems to grow according to the JMA law. When the glass is in the form of the thin-film, the crystals formed are different. The sequence of phases crystallized during the heat treatment is **(i)** from 870°C, the crystallization of $Ba_3Si_5O_{13}$ and $CaAl_2SiO_8$, **(ii)** from 960°C, $BaSiO_5$ major phase and the presence of the minor phase $CaAl_2SiO_8$. In this case, the glass melt is totally transformed during the formation of the first crystals, and the growth of the second generation of crystals is linear with the isothermal heating duration.

It is clear that the composition of the crystallized phases that are formed strongly depends on the geometry of the glass, and more particularly of the applied geometrical constraints. These constraints control the volume fraction of crystallized glass melt as a function of time and temperature, and thus modify the reactional pathways.

These findings open new possibilities for the formation of structured thin crystal layers. Indeed, by controlling thin-film glass thickness, glass composition, crystallization temperature and duration of the heat treatment, oriented thin films of crystals with controlled compositions, with possibly a controlled structuration at the nanoscale (using sequences of crystallization), can be prepared by glass melt crystallization. The pre-deposition of structured crystal nuclei networks on the substrate prior to the glass thin-film elaboration could also allow to control the location of the crystals' nucleation, the size of these crystals being controlled by the temperature / duration of the heat treatment parameters.

Acknowledgements

The authors wish to acknowledge Chevreul Institute (FR2638) and ULILLE for funding of NMR spectrometers.

References

[1] W. Höland, Biocompatible and bioactive glass-ceramics – state of the art and new directions, J. Non-Cryst. Solids 219 (1997) 192–197.

[2] L.L. Hench, D.E. Day, W. Höland, V.M. Rheinberger, Glass and Medicine, Int. J. Appl. Glass Sci. 1 (2010) 104–117.

[3] M.N. Rahaman, D.E. Day, B.S. Bal, Q. Fu, S.B. Jung, L.F. Bonewald, A.P. Tomsia, Bioactive glass in tissue engineering, Acta Biomater. 7 (2011) 2355–2373.

[4] L.C. Gerhardt, A.R. Boccaccini, Bioactive glass and glass-ceramic scaffolds for bone tissue engineering, Materials 3 (2010) 3867–3910.

[5] H. Hisakuni, K. Tanaka, Optical fabrication of micro lenses in chalcogenide glasses, Opt. Lett. 20 (1995) 958–960.

[6] B. Bureau, X.H. Zhang, F. Smektala, J.L. Adam, J. Troles, H. Li Ma, C. Boussard-Plèdel, J. Lucas, P. Lucas, D. Le Coq, M.R. Riley, J.H. Simmons, Recent advances in chalcogenide glasses, J. Non-Cryst. Solids 345–346 (2004)276–283.

[7] J.S. Sanghera, I.D. Aggarwal, Active and passive chalcogenide glass optical fibers for IR applications: a review, J. Non-Cryst. Solids 256–257 (1999) 6–16.

[8] M.L. Anne, J. Keirsse, V. Nazabal, K. Hyodo, S. Inoue, C. Boussard-Plèdel, H. Lhermite, J. Charrier, K. Yanakata, O. Loreal, J. Le Person, F. Colas, C. Compère, B. Bureau, Chalcogenide glass optical waveguides for infrared bio-sensing, Sensors 9 (2009) 7398–7411.

[9] B.J. Eggleton, B. Luther-Davies, K. Richardson, Chalcogenide photonics, Nat. Photonics. 5 (2011) 141–148.

[10] M.A. Green, Thin-film solar cells: review of materials, technologies and commercial status, J. Mater. Sci. Mater. Electron. 18 (2007) 15–19.

[11] L. Wang, C. Meng, C. Liu, L. Wang, Glass-ceramic protective coating for titanium alloys, J. Am. Ceram. Soc. 85 (2002) 2867–2869.

[12] G. Wang, H. Yang, J. Liang, Q. Chen, Preparation Methods and Application of Silicon Oxide Films, Atlantis Press, 2014, pp. 479–483.

[13] A.K. Varshneya, Fundamentals of Inorganic Glasses, first ed., Academic Press Boston, 1994.

[14] M. Engholm, L. Norin, D. Åberg, Strong UV absorption and visible luminescence in ytterbium-doped aluminosilicate glass under UV excitation, Opt. Lett. 32 (2007) 3352–3354.

[15] K.E. Youden, T. Grevatt, R.W. Eason, H.N. Rutt, R.S. Deol, G. Wylangowski, Pulsed Laser Deposition of Ga-La-S Chalcogenide Glass Thin Film Optical Waveguides, Appl. Phys. Lett. 63 (1993) 1601−1603.

[16] S. Mailis, C. Riziotis, J. Wang, E. Taylor, A.A. Anderson, S.J. Barrington, H. Rutt, R.W. Eason, N.A. Vainos, C. Grivas, Growth and Characterization of Pulsed Laser Deposited Lead Germanate Glass Optical Waveguides, Opt. Mater. 12 (1999) 27−33.

[17] K.D. Wise, R.H. Weissman, Thin Films of Glass and their Application to Biomedical Sensors, Med. Biol. Eng. 9 (1971) 339−350.

[18] K.I. Cho, S.H. Lee, K.H. Cho, D.W. Shin, Y.K. Sun, $Li_2OB_2O_3$-P_2O_5 Solid Electrolyte for Thin Film Batteries, J. Power Sources 163 (2006) 223−228.

[19] J. Sakurai, S. Hata, A. Shimokohbe, Novel Fabrication Method of Metallic Glass Thin Films Using Carousel Type Sputtering System, Proc. SPIE 5650 (2004) 260−267.

[20] G.E. Stan, D.A. Marcov, I. Pasuk, F. Miculescu, S. Pina, D.U. Tulyaganov, J. Ferreira, Bioactive Glass Thin Films Deposited by Magnetron Sputtering Technique: The Role of Working Pressure, Appl. Surf. Sci. 256 (2010) 7102−7110.

[21] G.E. Stan, D. Bojin, Adherent Glass-Ceramic Thin Layers with Bioactive Potential Deposited by Magnetron Sputtering Techniques, Sci. Bull. - Univ. “Politech.” - Bucharest, Ser. B 72 (2010) 187−196.

[22] S. Liste, P. González, J. Serra, J.P. Borrajo, S. Chiussi, B. León, M. Pérez-Amor, J.G. López, F.J. Ferrer, Y. Morilla, M.A. Respaldiza, Study of the Stoichiometry Transfer in Pulsed Laser Deposition of Bioactive Silica-Based Glasses, Thin Solid Films, 453−454 (2004) 219−223.

[23] S. Liste, J. Serra, P. González, J.P. Borrajo, S. Chiussi, B. León, M. Pérez-Amor, The Role of the Reactive Atmosphere in Pulsed Laser Deposition of Bioactive Glass Films, Thin Solid Films 453−454 (2004) 224−228.

[24] L. D'Alessio, R. Teghil, M. Zaccagnino, I. Zaccardo, D. Ferro, V. Marotta, Pulsed Laser Ablation and Deposition of Bioactive Glass as Coating Material for Biomedical Applications, Appl. Surf. Sci. 138−139 (1999) 527−532.

[25] S. Ishikawa, A. Urano, H. Aikawa, C. Hirose, H. Kanamori, M. Saitoh, Method for Producing Glass Thin Film, Patent US5660611, 1997.

[26] G.V. Bychko, V.A. Grozhik, Y.G. Zonov, Properties of Thin-Film Glass Coatings Produced by Laser Deposition in Vacuum, Glass Ceram. 56 (1999) 123−126.

[27] L.C. Chen, Particulates Generated by Pulsed Laser Ablation, in: D.B. Chrisey, G.K. Hubler (Eds.), Pulsed Laser Deposition of Thin Film, Wiley-VCH, New York, 2003; pp. 167−198.

[28] D.B. Chrisey, G.K. Hubler, Pulsed Laser Deposition of Thin Films, firth ed., Wiley-Interscience, New York, 1994.

[29] D. Coillot, F.O. Méar, R. Podor, L. Montagne, Autonomic Self-Repairing Glassy Materials, Adv. Funct. Mater. 20 (2010) 4371–4374.

[30] D. Coillot, F.O. Méar, R. Podor, L. Montagne, Characterization of self-healing glassy composites by high-temperature environmental scanning electron microscopy (HT-ESEM), J. Electron Micros. 59 (2010) 359–366.

[31] D. Coillot, F.O. Méar, R. Podor, L. Montagne, Influence of the Active Particles on the Self-Healing Efficiency in Glassy Matrix, Adv. Eng. Mater. 13 (2011) 426–435.

[32] S. Castanié, T. Carlier, F.O. Méar, S. Saitzek, J.F. Blach, R. Podor, L. Montagne, Self-Healing Glassy Thin Coating for High-Temperature Applications, Appl. Mater Interfaces, 8 (2016) 4208–4215.

[33] M. Avrami, Kinetics of Phase Change. I General Theory, J. Chem. Phys. 7 (1939) 1103–1112.

[34] N.P. Bansal, E.A. Gamble, Crystallization kinetics of a solid oxide fuel cell seal glass by differential thermal analysis, J. Power Sources 147 (2005) 107–115.

[35] G. Wu, Q.H. Tang, N.N. Yu, X.S. Miao, Phase separation and nanocrystallization behavior above crystallization temperature in Mg-Cu-Y metallic glass thin film, Thin Solid Films 545 (2013) 38–43.

[36] K. White, R.L. Crane, J.A. Snide, Crystallization kinetics of As-Sb-S glass in bulk and thin film form, J. Non-Cryst. Solids 103 (1988) 210–220.

[37] T. Carlier, S. Saitzek, F.O. Méar, J.F. Blach, A. Ferry, M. Huvé, L. Montagne, Aluminosilicate glass thin films elaborated by pulsed laser deposition, Appl. Surf. Sci. 397 (2017) 13–18.

[38] C.A. Schneider, W.S. Rasband, K.W. Eliceiri KW, NIH Image to ImageJ: 25 years of image analysis, Nat Methods. 9 (2010) 671–675.

[39] D. [Lowe, Distinctive Image Features from Scale-Invariant Keypoints, Inter. J. Computer Vision, 60 (2004) 91–110.

[40] I. Arganda-Carreras, V. Kaynig, C. Rueden, K.W. Eliceiri, J. Schindelin, A. Cardona, H.Sebastian Seung, Trainable Weka Segmentation: a machine learning tool for microscopy pixel classification, Bioinformatics 33 (2017) 2424–2426.

[41] P. Namwrong, N. Laorodphan, W. Thiemsorn, M. Jaimasith, A. Wannakon, T. Chairuangsri, A Barium-Calcium Silicate Glass for Use as Seals in Planar SOFCs, Chiang Mai J. Sci. 37 (2010) 231–242.

[42] J.W. Fergus, Sealants for solid oxide fuel cells, J. Power Sources 147 (2005) 46–57.

[43] A. Kremenovic, J. Djordjevic, V. Dondur, R. Dimitrijevic, Structural investigations of celsian glass derived from Ba-LTA zeolite, Phys. Chem. Chem. Phys. 3 (2001) 1560–1565.

[44] G.P. Kothiyal, M. Goswami, B. Tiwari, K. Sharma, A. Ananthanarayanan, L. Montagne, Some recent studies on glass/glass-ceramics for use as sealants with special emphasis for high temperature applications, J. Adv. Ceram. 2 (2012) 110–129.

[45] G. Libourel, C.A. Geiger, L. Merwin, A. Sebald, ^{29}Si and ^{27}Al MAS-NMR spectroscopy of glasses in the system $CaSiO_3$-$MgSiO_3$-Al_2O_3, Chemical Geology, 96 (1992) 387–397.

[46] L. Rezazadeh, S. Baghshahi, A. Nozad Golikand, Z. Hamnabard, Structure, phase formation, and wetting behaviorof BaO-SiO_2-B_2O_3 based glass-ceramics as sealants for solid oxide fuel cells, Ionics 20 (2014) 55–64.

[47] N.P. Bansal, E. Gambel, Crystallization kinetics of a solid oxide fuel cell seal glass by differential thermal analysis, J. Power Sources 147 (2005) 107–115.

[48] B.O. Mysen, D. Virgo, F.A. Seifert, The structure of silicate melts: Implications for chemical and physical properties of natural magma, Rev. Geophys. Space Phys. 20 (1982) 353–383.

Tables & Figures Caption

Table 1: Characteristic of the BCAS glass.

Figure 1. (a) Schematic view of glass thin-film on Si-substrate; **(b)** TEM image showing the amorphous nature of BCAS glass thin-film deposited on crystalized Si-substrate.

Figure 2. Heat treatment performed during in-situ monitoring of crystallization by HT-XRD.

Figure 3. (a) XRD patterns showing the crystallization of BCAS bulk glass vs. temperature and time; **(b)** Identification of crystallized phases formed at different times heat treatment of BCAS bulk glass powder.

Figure 4. ^{29}Si and ^{27}Al NMR spectra of BCAS bulk glass before (^{29}Si NMR (a) & ^{27}Al NMR (c)) and after heat treatment (10h at 970°C) (^{29}Si NMR (b) & ^{27}Al NMR (d)).

Figure 5. HT-ESEM micrographs showing the crystallization phases shapes of bulk BCAS glass vs. temperature and time at 1070°C. **(a)** General view of the sample; **(b)** Image series showing the first crystallization at the sample surface; **(c)** Image series showing the second crystallization at the sample surface; **(d)** Image series showing the third crystallization at 1070°C.

Figure 6. Variation of the area covered by crystals as a function of time and temperature. Data for glass bulk are reported with squares, associated temperature being in white squares. The data for the thin film are reported with circles (white circles = first precipitation of crystals; grey circles = second precipitation of crystals), associated temperature in black circles.

Figure 7. (a) XRD patterns showing the crystallization of BCAS glass thin-film vs. temperature and time; **(b)** Identification of crystallized phases formed at different times heat treatment of BCAS glass thin-film.

Figure 8. HT-ESEM micrographs showing the crystallization phases shapes of BCAS glass thin-film vs. temperature and time at 960°C.

Figure 9. Evolution of the sample surface coverage by the grown $BaSi_2O_5$ crystals as a function of time at 1000°C. The basis corresponds to the first crystallization. The upper part corresponds to the second crystallization.

Figure 10. (a) Schematic representation of the Q^n species in a Ca-Ba-aluminosilicate glass; **(b)** Summary of the crystallized phases obtained during the heat treatment at T_x as a function of time of the BCAS bulk glass and thin-layer, highlighting the Q^n species evolution as a function of temperature.

Supplementary Files Caption

Suppl. File 1. Glass Bulk-First Recristallisation-X10000.

Suppl. File 2. Glass Bulk-Second and third crystallisation-X2500.

Suppl. File 3. Glass Bulk-Second and third crystallisation-X1000.

Suppl. File 4. Thin Film-First and second crystallisation-X10000.

Suppl. File 5. Thin Film-First and second crystallisation-3D view.

Table 1. Characteristic of the BCAS glass.

Measured glass composition (mol.%)	**T_g (°C)**	**T_x (°C)**	**T_c (°C)**	**$(T_x - T_g) / T_x$**
28.6BaO-14.3CaO-9.5Al_2O_3-47.6SiO_2	750 ± 2	970 ± 2	1070 ± 2	0.23

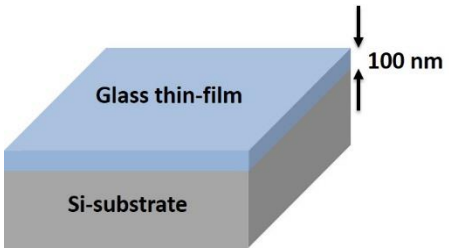

(a)

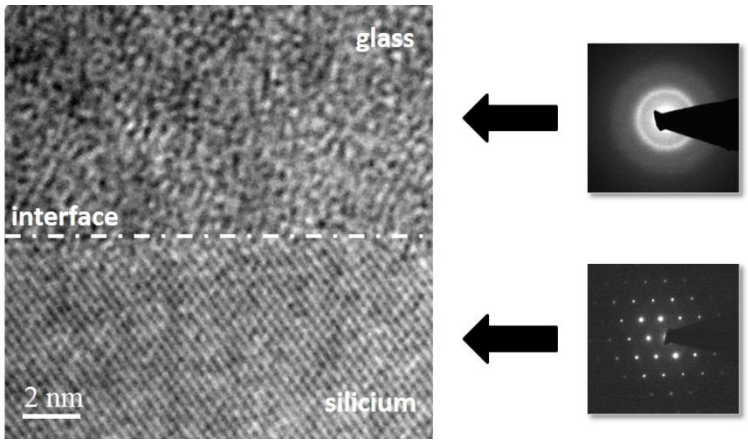

(b)

Figure 1. (a) Schematic view of glass thin-film on Si-substrate; **(b)** TEM image showing the amorphous nature of BCAS glass thin-film deposited on crystallized Si-substrate.

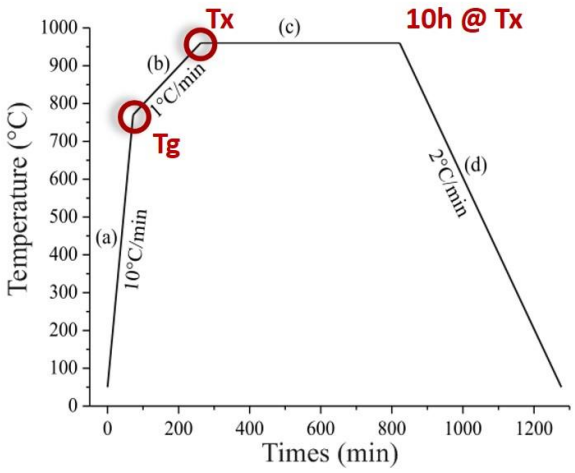

Figure 2. Heat treatment performed during in-situ monitoring of crystallization by HT-XRD.

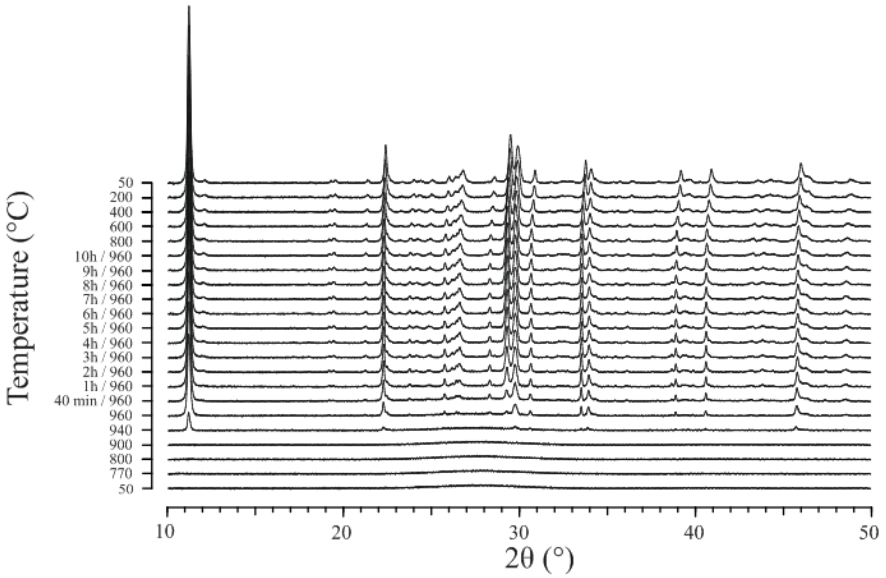

(a)

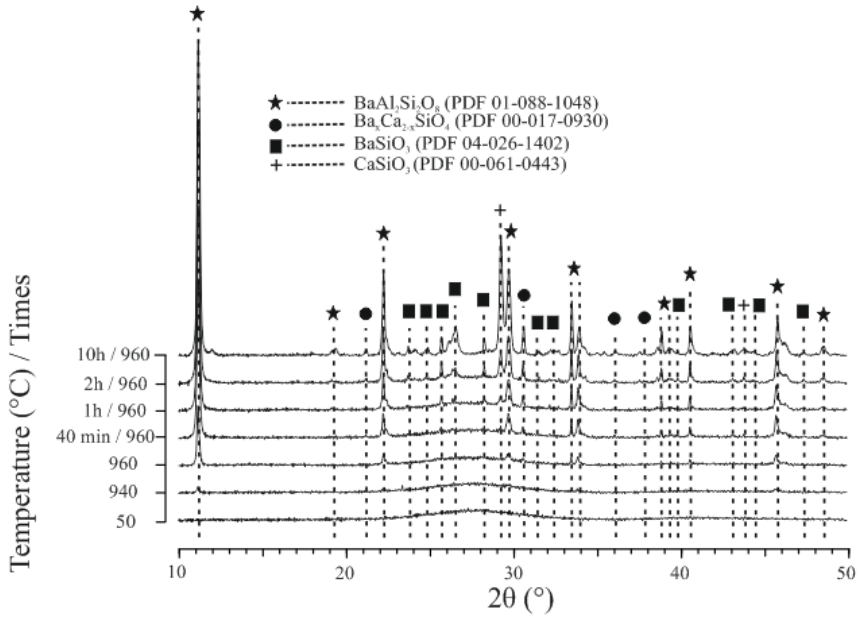

(b)

Figure 3. (a) XRD patterns showing the crystallization of BCAS bulk glass vs. temperature and time; **(b)** Identification of crystallized phases formed at different times heat treatment of BCAS bulk glass powder.

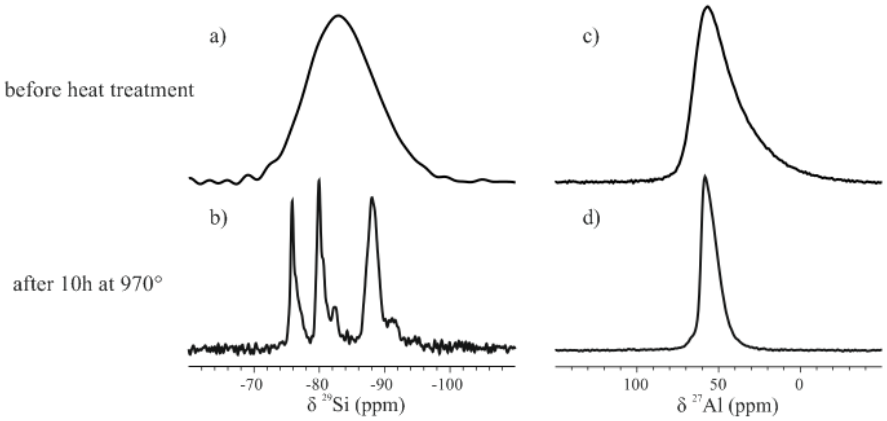

Figure 4. ^{29}Si and ^{27}Al NMR spectra of BCAS bulk glass before (^{29}Si NMR (a) & ^{27}Al NMR (c)) and after heat treatment (10h at 970°C) (^{29}Si NMR (b) & ^{27}Al NMR (d)).

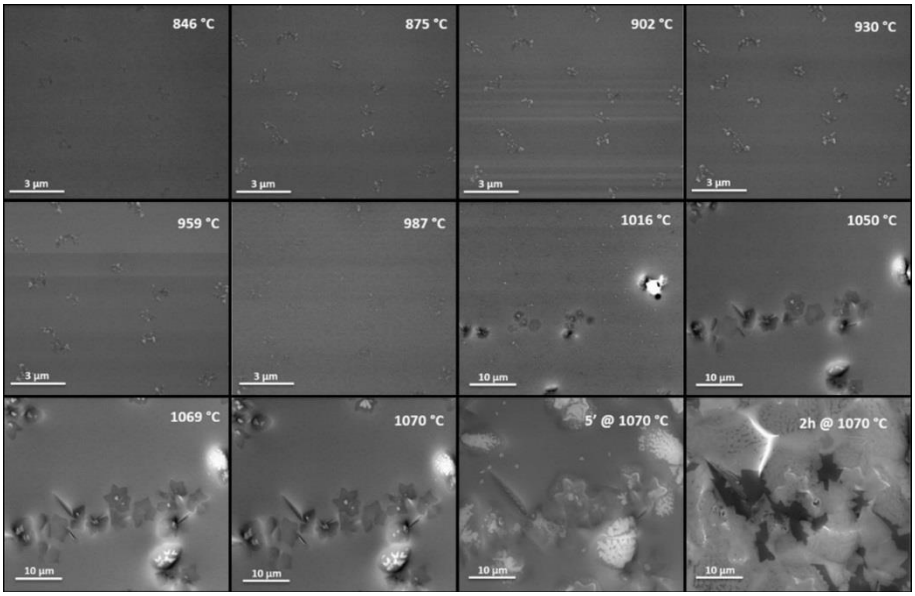

(a)

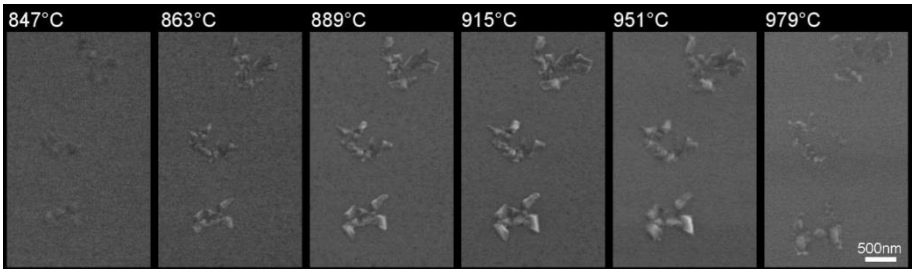

(b)

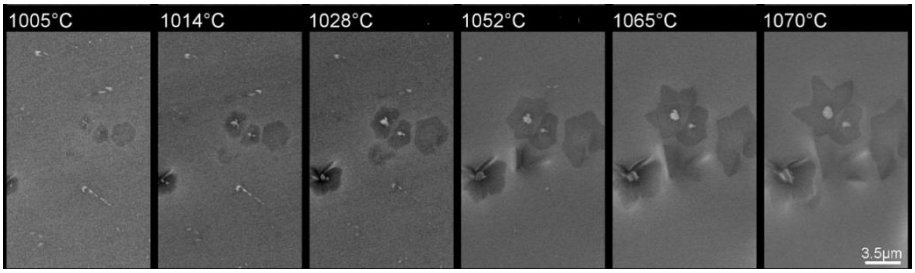

(c)

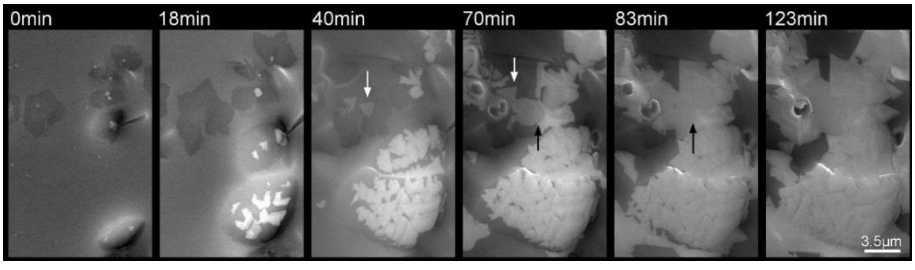

(d)

Figure 5. HT-ESEM micrographs showing the crystallization phases shapes of bulk BCAS glass vs. temperature and time at 1070°C. **(a)** General view of the sample; **(b)** Image series showing the first

crystallization at the sample surface; **(c)** Image series showing the second crystallization at the sample surface; **(d)** Image series showing the third crystallization at 1070°C.

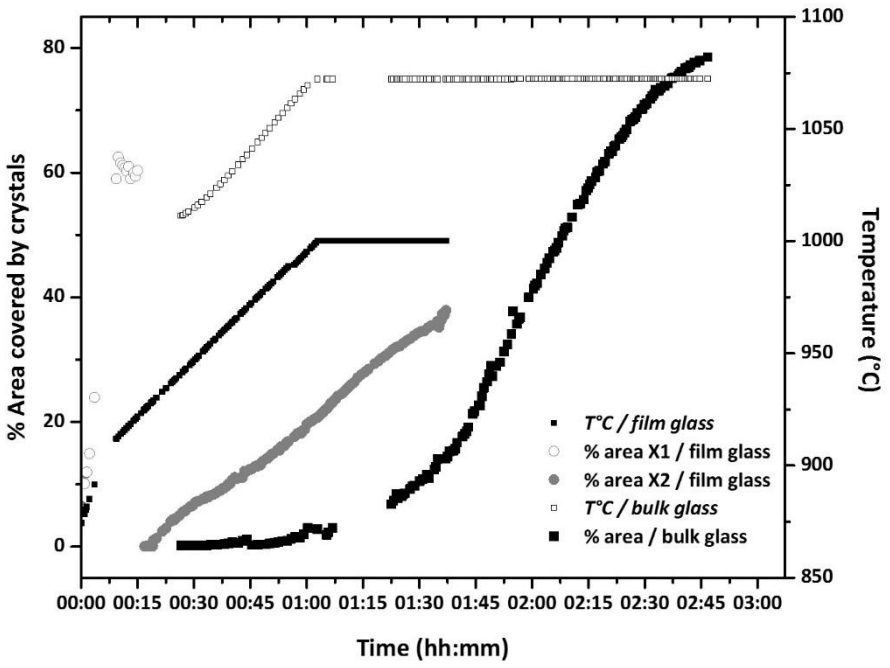

Figure 6. Variation of the area covered by crystals as a function of time and temperature. Data for glass bulk are reported with squares, associated temperature being in white squares. The data for the thin film are reported with circles (white circles = first precipitation of crystals; grey circles = second precipitation of crystals), associated temperature in black circles.

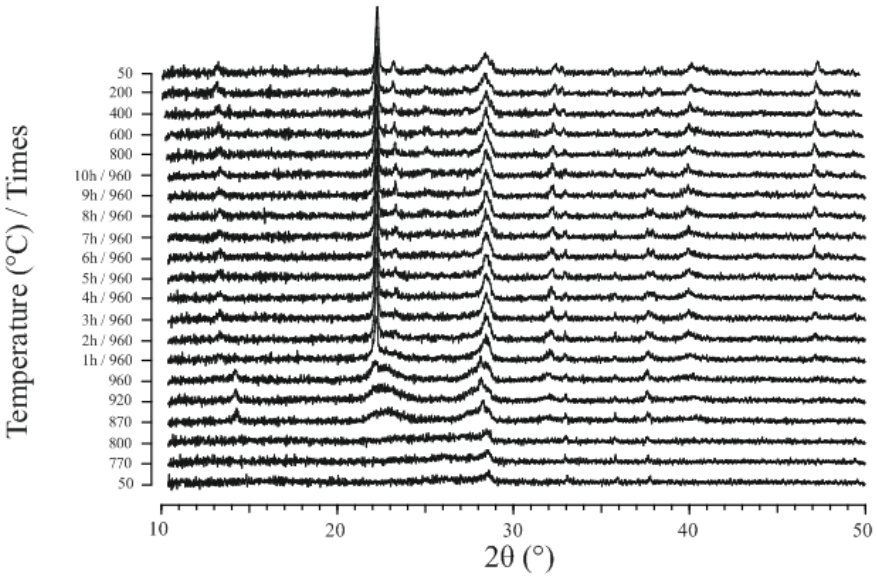

(a)

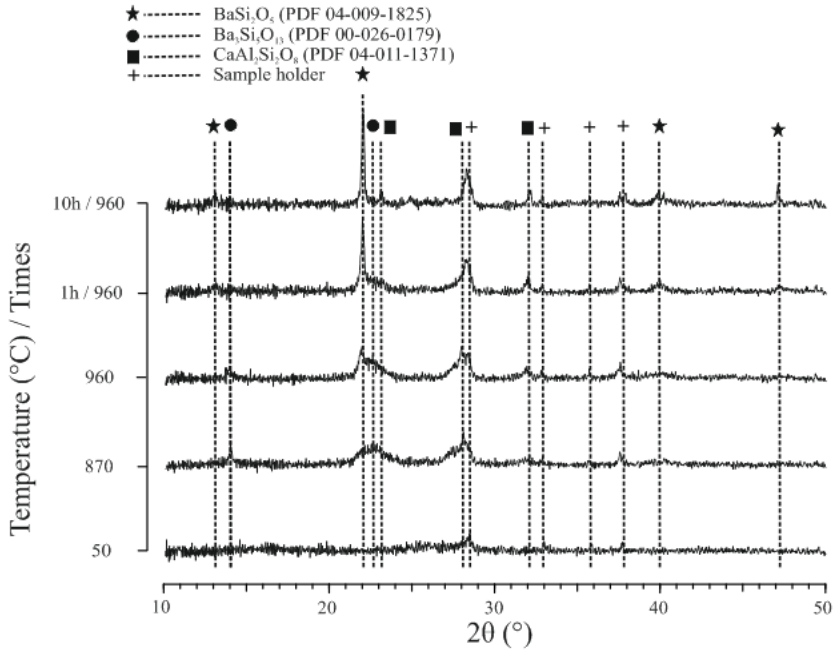

(b)

Figure 7. (a) XRD patterns showing the crystallization of BCAS glass thin-film vs. temperature and time; **(b)** Identification of crystallized phases formed at different times heat treatment of BCAS glass thin-film.

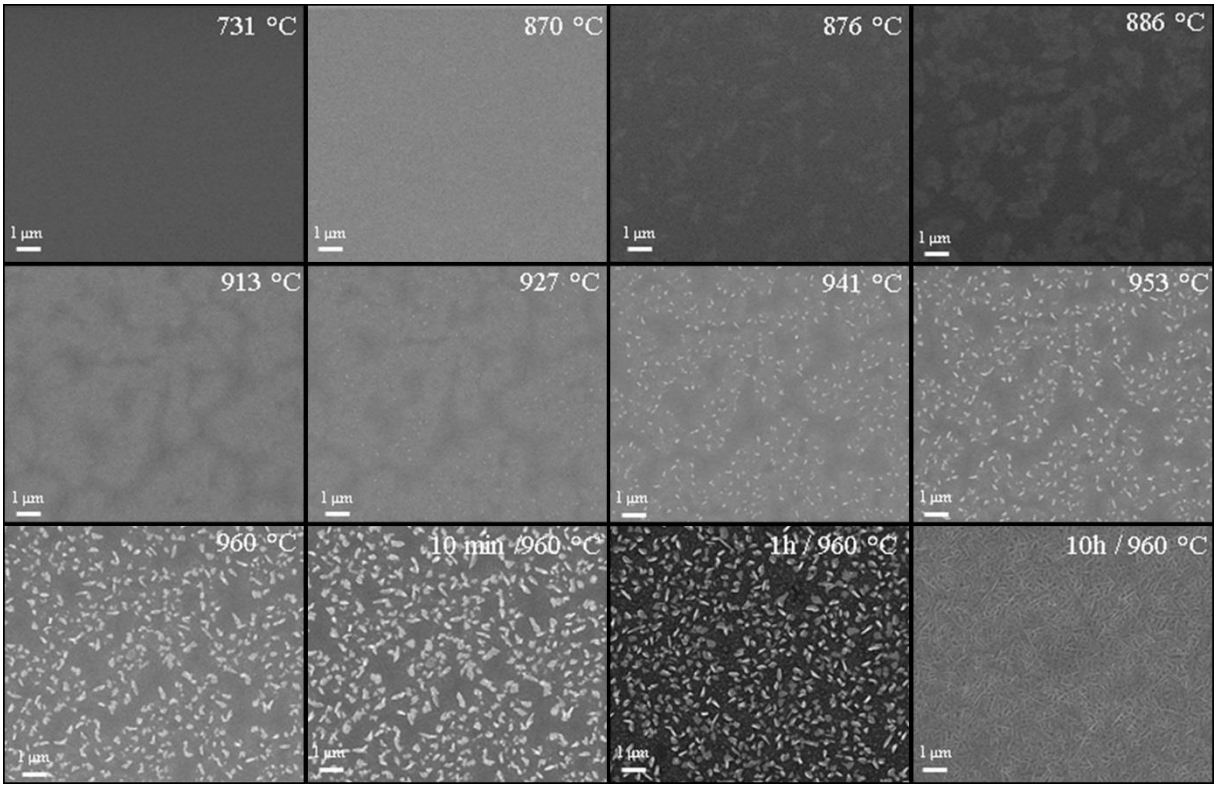

Figure 8. HT-ESEM micrographs showing the crystallization phases shapes of BCAS glass thin-film vs. temperature and time at 960°C.

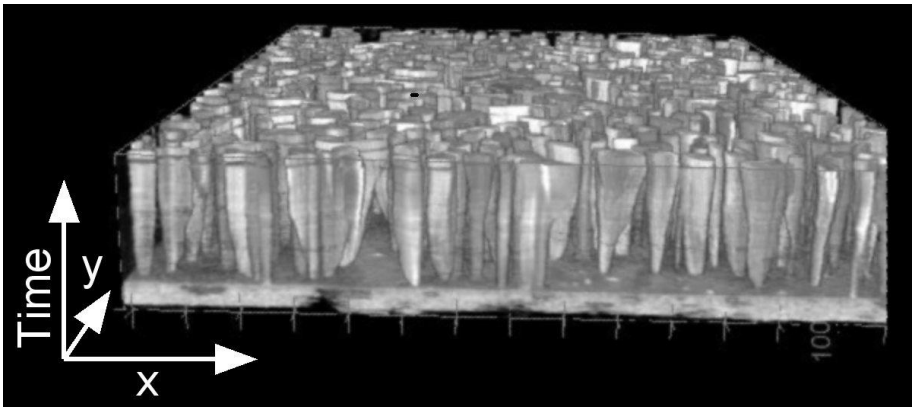

Figure 9. Evolution of the sample surface coverage by the grown $BaSi_2O_5$ crystals as a function of time at 1000°C. The basis corresponds to the first crystallization. The upper part corresponds to the second crystallization.

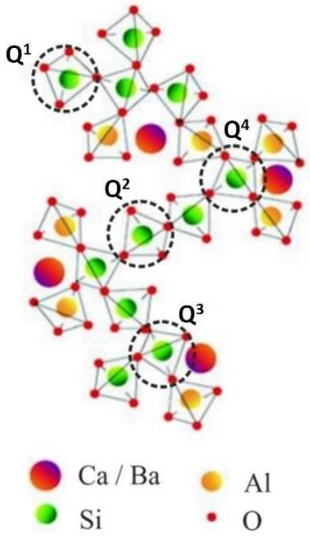

(a)

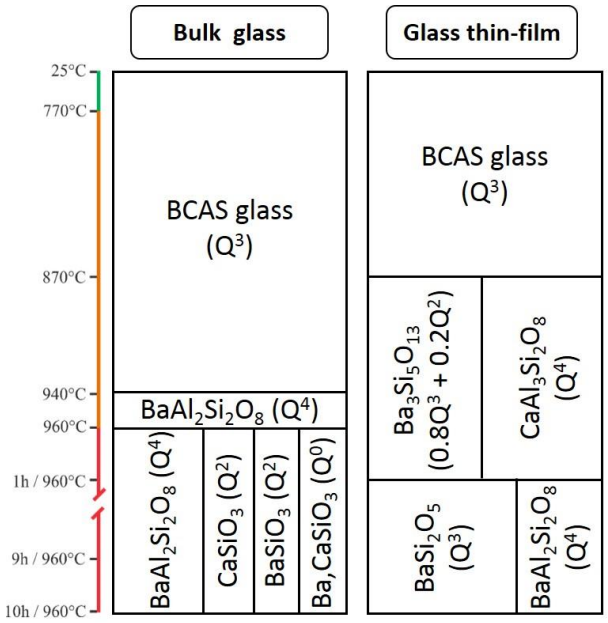

(b)

Figure 10. (a) Schematic representation of the Q^n species in a Ca-Ba-aluminosilicate glass; **(b)** Summary of the crystallized phases obtained during the heat treatment at T_x as a function of time of the BCAS bulk glass and thin-layer, highlighting the Q^n species evolution as a function of temperature.